ELSEVIER

Journal of Biomechanics 37 (2004) 55–65

JOURNAL OF BIOMECHANICS

www.elsevier.com/locate/jbiomech
www.JBiomech.com

Time-lapsed microstructural imaging of bone failure behavior ☆

Ara Nazarian[a,b], Ralph Müller[a,b,*]

[a] *Institute for Biomedical Engineering, Swiss Federal Institute of Technology (ETH) and University of Zürich, Moussonstrasse 18, Zürich 8044, Switzerland*

[b] *Orthopedic Biomechanics Laboratory, Beth Israel Deaconess Medical Center, Harvard Medical School, Boston, USA*

Accepted 23 June 2003

Abstract

Many bones within the axial and appendicular skeleton are subjected to repetitive loading during the course of ordinary daily activities. If this loading is of sufficient magnitude or duration, failure of the bone tissue may result. Until recently the structural analysis of these fractures has been limited to two-dimensional sections. Due to the inherent destructiveness of this method, dynamic assessment of fracture progression has not been possible. An image-guided technique to analyze structural failure has been developed utilizing step-wise micro-compression in combination with time-lapsed micro-computed tomographic imaging. This technique allows, for the first time, direct three-dimensional visualization and quantification of fracture initiation and progression on the microscopic level and relates the global failure properties of trabecular bone to those of the individual trabeculae. The goals of this project were first to design and fabricate a novel micro-mechanical testing system, composed of a micro-compression device and a material testing and data acquisition system; and second, to validate the testing system to perform step-wise testing of trabecular bone specimens based on image-guided failure analysis. Due to the rate dependant properties of bone, stress relaxation was a concerning factor with respect to the step-wise testing method. In order to address these concerns, the results of the step-wise testing method were compared to those obtained from a conventional continuous test (considered to be the gold standard for the step-wise compressive mechanical testing) over the same total strain range and testing conditions. This was performed using porous aluminum alloy samples with highly reproducible and homogenous structural properties as well as trabecular bone samples from a single whale vertebra. Five cylinders from aluminum foam and trabecular whale bone each were compressed and imaged in a step-wise fashion from 0% to 20% strain at intervals of 2%, 4%, 8%, 12%, 16% and 20%. Mechanical properties obtained from the continuous and step-wise methods were not significantly different for both aluminum foam and whale bone specimens ($p > 0.05$). Both testing methods yielded very similar stress–strain graphs with almost identical elastic and plastic regions with overlaying standard error bars for both whale bone and aluminum foam specimens. This was further concurred by performing regression analyses between the stress data from both testing methods ($r^2 = 0.98$ for whale bone and aluminum foam specimens). Animations of fracture initiation and progression revealed that failure always occurred in local bands with the remaining regions of the structure largely unaffected independent of structure type. In conclusion, we found step-wise micro-compression to be a valid approach for image-guided failure assessment (IGFA) with high precision and accuracy as compared to classical continuous testing. We expect findings from upcoming studies of IGFA of human vertebral bone to improve our understanding of the relative importance of densitometric, morphological, and loading factors in the etiology of spontaneous fractures of the spine. Eventually, this improved understanding may lead to more successful approaches to the prevention of age-related fatigue fractures.

Keywords: Micro-computed tomography (μCT); Microstructural bone failure; Bone architecture; Bone failure; Time-lapsed imaging

1. Introduction

Osteoporosis, which occurs most frequently in post-menopausal women and the aged, is defined as a systemic skeletal disease characterized by low bone mass and architectural deterioration of bone tissue, with a concomitant increase in bone fragility and fracture risk (Kanis, 1994; Kleerekoper et al., 1985). Due to the

☆ Supplementary data associated with this article can be found at doi:10.1016/S0021-9290(03)00254-9.

*Corresponding author. Institute for Biomedical Engineering, Swiss Federal Institute of Technology (ETH) and University of Zürich, Moussonstrasse 18, Zürich 8044, Switzerland. Tel.: +41-1-632-4592; fax: +41-1-632-1214.

E-mail address: rmueller@biomed.ee.ethz.ch (R. Müller).

0021-9290/$ - see front matter © 2003 Elsevier Ltd. All rights reserved.
doi:10.1016/S0021-9290(03)00254-9

dominant presence of trabecular bone in vertebral bodies, up to 90% of the load in lumbar vertebrae is carried by trabecular bone (McBroom et al., 1985; Silva et al., 1997) most likely in a predominantly compressive mode. Therefore, an extended understanding of the failure behavior of trabecular bone is essential for estimating the risk of vertebral fractures. The increased use of densitometry throughout the last decade resulted in a focus on bone density as the most important predictor of osteoporotic bone fractures. Although many elderly people may lose bone, as expressed by a decrease in bone density, not all develop fractures. On an individual basis, density alone accounts for 10–90% of the variation in strength of trabecular bone (Ciarelli et al., 1991). This also means that 90–10% of the variation in strength cannot be explained by bone density. It has been shown that changes in trabecular morphology lead to a disproportionate decrease in bone strength (Goldstein, 1987). For this reason, microstructural information must be included in the analysis to predict individual mechanical bone properties (Mosekilde, 1988; Parfitt, 1987). However, the relative importance of bone density and architecture in the etiology of bone fractures is poorly understood.

Until recently fracture analysis was limited to two-dimensional sections to illustrate global fracture patterns (Choi and Goldstein, 1992; Crowell et al., 1993; Michel et al., 1993; Norrdin et al., 1998). Due to their inherent destructiveness, such procedures can only be used for static assessment of the fractured state and would not allow quasi-dynamic assessment of fracture progression. Image-guided failure assessment (IGFA) is a new technique that allows three-dimensional progressive analysis of bone fractures (Müller et al., 1998). The technique can be used to non-invasively monitor and evaluate fracture initiation and progression on the microscopic level as well as to determine how bone architecture influences bone failure. Despite the fact that the importance of trabecular structural parameters in explaining the overall mechanical properties of trabecular bone has been established, little is known regarding the failure modes and properties of individual trabeculae, and their relationship with global failure properties of trabecular bone.

IGFA involves the use of a micro-compression device (MCD) to apply and maintain strain, and the use of micro-computed tomography (μCT) to image the specimens in a given strain configuration (Müller et al., 1998). Using MCD and μCT, the specimen is compressed and imaged in a time-lapsed fashion, allowing the assessment of fracture initiation and progression not only in the elastic region but also beyond yield in the plastic region. However, before the technique can be used to study human bone failure, proper validation is needed. In the original implementation (Müller et al., 1998), the MCD was loaded using a commercial servo-hydraulic compression device causing problems in locking in the applied strain for the duration of imaging. Therefore, the goals of this project were first, to design and fabricate a novel micro-mechanical testing system, composed of a MCD and a custom-made material testing and data acquisition system (MTDAQ), and second, to determine the precision and accuracy of time-lapsed IGFA in highly reproducible aluminum foams as well as trabecular bone samples from a single whale vertebral body.

2. Materials and methods

2.1. Specimen preparation

In order to assess the reproducibility and accuracy of the micro-compression test, two types of cellular solid materials, engineered and biological, were used for the validation purposes. For the engineered samples, three groups of ten cylinders (8 mm in diameter and 16 mm in length; in accordance with recommendations for testing bone specimens using a 2:1 ratio between length and diameter (Keaveny et al., 1993a) were fabricated from highly porous aluminum alloys (Duocel 6101-T6, ERG, Oakland, CA) with volume densities of 4%, 8% and 12%, respectively. The porous alloy was used because its anisotropic and inhomogeneous nature is very similar to that of human trabecular bone, our actual target material for IGFA. Additionally, these engineered structures with volume densities of 4%, 8% and 12% exhibit high similarities to trabecular bone found in the human lumbar spine, which has average volume densities of $9\pm3\%$ (Hildebrand et al., 1999). The morphologic analogy between these two structures is best shown in the three-dimensional visualizations depicted in Fig. 1. It is noteworthy that these foams are compared to bone in terms of their morphology and not in terms of the mechanical properties of the aluminum alloys. For the biological samples, additional ten trabecular bone specimens were obtained from a single bowhead whale vertebral body. Due to the large size of the vertebra (400 mm in diameter and 200 mm in height) and the large regions of highly homogenous, uniformly oriented trabecular bone, whale vertebral bodies are ideal sources of obtaining relatively large batches of specimens with similar trabecular architecture and density. Human vertebral bodies typically show much higher variation in the trabecular bone structure and density due to their relatively small size and the considerable variation in bone architecture between humans. The whale vertebral body was preserved in saline-soaked gauze at a temperature of $-20^{\circ}C$. The specimens were cored out of a pre-cut block of the vertebral body using a diamond coring-tool parallel to the direction of the anatomical axis (Starlite Industries,

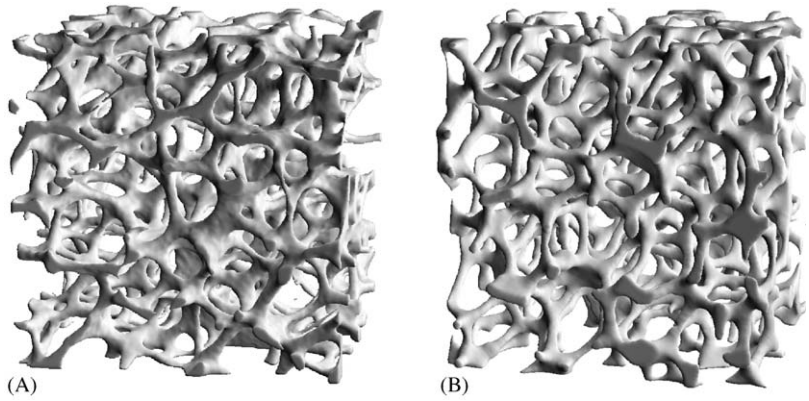

Fig. 1. (A) Three-dimensional trabecular bone architecture of a lumbar spine bone biopsy of a 42-year-old male ($4 \times 4 \times 4\,mm^3$); (B) three-dimensional architecture of Duocel aluminum alloy ($8 \times 8 \times 8\,mm^3$). The structural similarities between the bone and the aluminum foam can easily be seen.

Rosemont, PA) while completely submerged in 0.9% saline solution. The two ends of the cored samples were then cut perpendicular to the anatomical axis of the trabeculae between two parallel diamond wafering blades running on a low-speed saw (Isomet, Buehler Corp., Lake Bluff, IL) and operating under copious irrigation. The above precautionary measures were taken in order to minimize the disruption of the trabecular network, hence minimizing the damage artifacts at both ends of the specimens and maintaining full hydration during all stages of preparation.

Both the aluminum foam and trabecular bone specimens were randomly assigned to two groups of five specimens each designated for step-wise or continuous testing, respectively. Weights, lengths, and apparent densities of the step-wise and continuous samples were checked for differences between the two groups, and no statistical differences were found. The coefficient of variation (CV) for apparent density ranged from 2.5% for the aluminum cylinders and 4.7% for the whale bone specimens, respectively. Before testing, pre-aligned brass end caps with a 9 mm diameter and 0.5 mm thickness were glued with cyanoacrylate (American Glue Corp., Taylor, MI) to both ends of the specimen. This restrained displacements at the ends of the sample and effectively reduced end artifacts (Keaveny et al., 1993b) by providing support to the free ends of the trabeculae. Prior to mechanical testing all whale trabecular specimens were thawed over night in a 0.9% saline solution, and the tests were conducted at room temperature. The specimens remained wet during testing, where humidity was sealed within the MCD. This was verified upon retrieval of wet specimens at the end of each test.

2.2. Micro-mechanical testing system

In order to visualize material failure on a micro-structural level, a novel micro-mechanical testing system was devised to measure loaded porous materials directly in the μCT. The micro-mechanical testing system consisted of two major components, the MCD and the material testing and data acquisition (MTDAQ) system, designed to provide uniaxial compression, data acquisition, and strain locking of the specimen during imaging. The MCD was designed to house the test specimens and act as a transportable link between the mechanical testing and μCT imaging steps. Its duties were to hold the specimen, lock the applied strain to the specimen, record the applied load via an onboard load-cell, and provide a radiolucent window for scanning of the specimen (Fig. 2). The radiolucent window was manufactured from Torlon 4203 with excellent dimensional stability and an order of magnitude larger yield strength and modulus of elasticity values than those of the aluminum foam and trabecular bone. The dimensions of the Torlon piece was measured multiple times after successive testing to verify their dimensional stability. The load cell (SMD Sensors, Meriden, CT) with dimensions small enough to fit inside the base of the MCD was rated for 2225 N with a nonlinearity of ± 2.225 N and a repeatability of 0.667 N. The size of the specimen chamber was $\varnothing$ 9 mm × 22 mm capable of holding wet and dry bone specimens. The overall dimensions of the MCD were $\varnothing$ 19 mm × 65 mm to meet the spatial restriction of the μCT bore. Previously, the MCD was loaded axially via a standard mechanical testing device (Müller et al., 1998). The axial strain was applied through a pushpin on the MCD cap and the applied strain was locked manually. This combination introduced errors in the form of strain application fluctuation, due to reduced sensitivity of standard mechanical testing devices at small strains, and the application of unknown manual torque in the strain locking process.

In order to alleviate these problems, the MCD was instead interfaced with the newly designed MTDAQ to

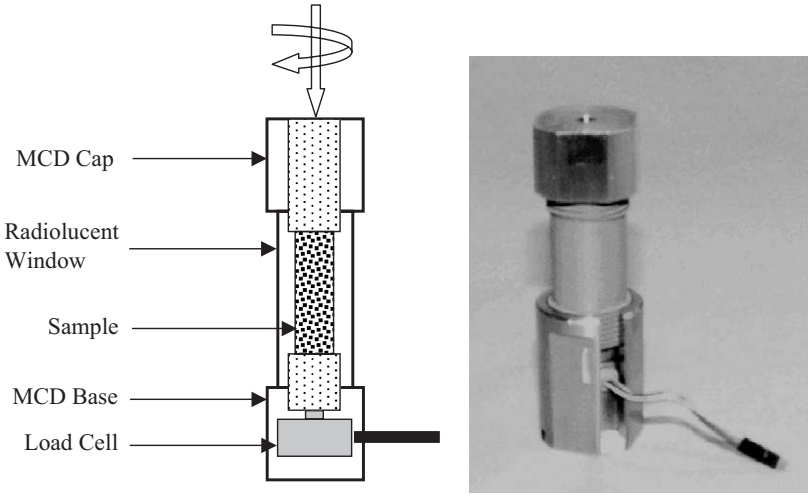

Fig. 2. Schematic drawing and photograph of MCD. The MCD is used both to apply forces to the sample and to hold and preserve the sample during scanning.

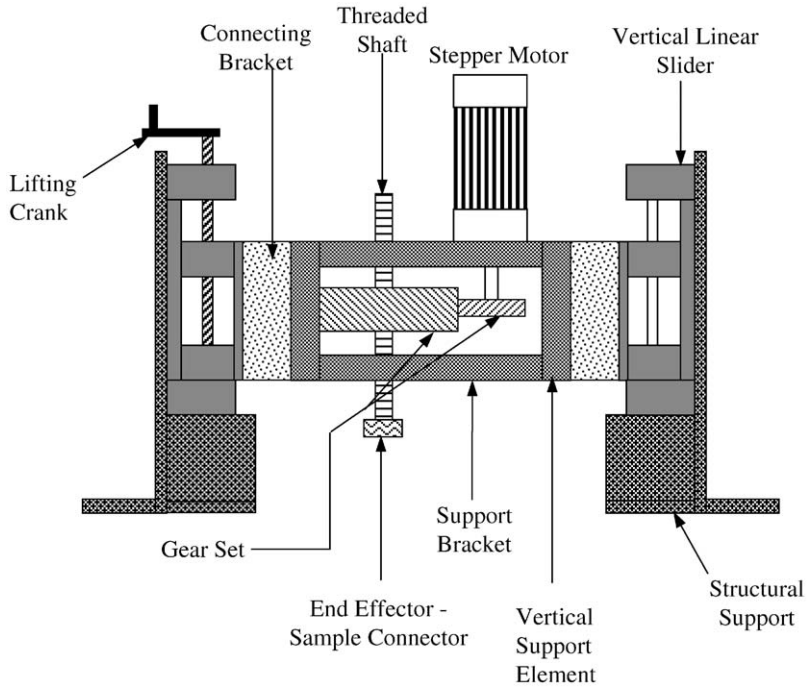

Fig. 3. Schematic drawing of mechanical testing and data acquisition (MTDAQ) system. The MTDAQ is a specialized micromechanical system that allows for the application highly precise torque and displacement to the MCD.

apply translational linear strain generated from rotational motion by means of a screw driven micro-stepping actuator. The stepper motor (HT34-438, Applied Motion Products, Watsonville, CA) provided 15 N m torque with 200 steps per revolution. It was controlled by a micro-stepping drive/indexer (OEM ZL6104, Parker Automation, Rohnert Park, CA) capable of subdividing each stepper motor step into 125 micro-steps. The advantages of this feature were the increased number of steps for refined rotational control and smoother motion. Also, an encoder (755A, Encoder Products, Sandpoint ID) was used to create a closed loop feedback system for proper control, accurate motor position and velocity maintenance. The overall components of the system (Fig. 3) were the stepper motor, the micro-stepping drive/indexer, the threaded shaft, the gear set, the vertical linear slide, the linear variable differential transformer (LVDT), the mounting bracket for the MCD and the structural support elements and brackets. An onboard LVDT (100 MHR, Shaevitz Sensors, Hampton, VA), rated for a range of ± 2.54 mm with a resolution of 1 μm and a non-linearity of ± 3.8 μm measured the applied strain to the specimen. The LVDT was attached to the end effector, hence

measuring the total strain. In order to receive the load and displacement signals, a PCI-MIO-16E4 (National Instruments, Austin, TX) data acquisition board with a 250 kb/s sampling rate, 12-bit resolution, and eight differential input channels was used. The data acquisition board was connected to a PC for control of the system using Labview (National Instruments, Austin, TX) control and acquisition software.

For the actual mechanical testing, half of the aluminum and whale cylinders were compressed continuously from 0% to 20% strain at a strain rate of $0.01\,s^{-1}$ using MCD in combination with the MTDAQ. The remainder of the specimens were imaged and compressed step-wise at intervals of 0%, 2%, 4%, 8%, 12%, 16% and 20% strain. Each specimen was placed inside the MCD and preconditioned between 0.0% and 0.3% at a rate of $0.005\,s^{-1}$ to eliminate typical toe behavior (Keaveny et al., 1994). Then, the specimen was transferred to the μCT for initial imaging of the sample in the intact state (0%). After imaging, the specimen was returned to the MTDAQ, and exposed to a first monocyclic nominal strain of 2% in order to capture the linear and yield behavior of the material. Following the application of each strain step, the specimen was allowed to relax for 20 min prior to its transfer to the μCT for imaging. The 20-min window was chosen based on experiments performed to establish an appropriate time interval for specimens to reach a plateau for stress relaxation. This procedure was repeated five more times to acquire additional time-lapsed images of 4%, 8%, 12%, 16% and 20% nominal strain in the post-failure regime, where each imaging step took approximately 90 min.

Due to the discontinuous nature of the step-wise testing method, and the stress relaxation occurring in the specimen between two measurement segments, the step-wise stress–strain graphs consisted of six discontinuous sections between the seven strain steps from 0% to 20% strain. In order to again introduce continuity in the graphs, straight lines were added to the discontinuous regions, based on the assumption that the results obtained from the reconstructed step-wise tests would be compatible with those obtained from continuous tests. In other words, a straight line was fitted from the end of one strain step to a point on the next strain step. This was an arbitrary measure to create continuous graphs from the step-wise data. The introduction of the above mentioned lines to the graph are considered as part of the technique at this stage. The validation results are used to address whether the addition of these lines resulted in a method (step-wise) capable of proper reflection of mechanical properties of the specimens as explained in the continuous test.

The raw data was resampled and averaged to obtain stresses between 0% and 2% strain at intervals of 0.2% strain and between 2% and 20% strain at intervals of 1% strain. This data was used to determine statistical differences between the loads of the step-wise and continuous tests at corresponding strains and to determine the correlation between the step-wise and continuous loads. Modulus of elasticity, stiffness, yield strain and strength, ultimate strain, strength and load were calculated and statistical differences were assessed for the two loading regimens using a two-tailed Student's *t*-tests. Ultimate load and strain were defined as the initial peak load and its corresponding strain, respectively. The images for the step-wise compressions of aluminum foam and whale bone cylinders were compared at corresponding strains using three-dimensional visualizations and animations to allow a qualitative description of the failure mechanisms.

2.3. Micro-tomographic imaging

Images were generated using a micro-tomographic imaging system (μCT 20, Scanco Medical, Bassersdorf, Switzerland), a compact fan-beam type tomograph, also referred to as desktop μCT (Rüegsegger et al., 1996). This specific system provides an isotropic spatial resolution of 28 μm and has been used extensively for different research projects involving the assessment and analysis of microstructural bone and porous materials (Müller and Rüegsegger, 1997).

For the purpose of this study, a total of 510 micro-tomographic slices were acquired for both the aluminum and bone cylinders. Measurements were stored in three-dimensional image arrays with isotropic voxel sizes of 34 μm. Total examination time per specimen approached 90 min. A three-dimensional Gaussian filter with a limited, finite filter support was used to partly suppress the noise in the volumes. In the next step, alloy or bone was segmented from background with the help of a global thresholding procedure (Müller and Rüegsegger, 1997). Samples were binarized using the same parameters for the filter width (1.2), the filter support (1) and the threshold, which were 286‰ of the maximum gray scale value for aluminum and 320‰ for bone, respectively.

3. Results

Mean and standard deviations of the mechanical properties of step-wise and continuously compressed aluminum and bone cylinders are given in Tables 1 and 2, respectively. The CV for the bone properties varied from 5% to 28% for the continuous specimens and from 5% to 31% for step-wise specimens. The CVs of the properties for the 4% apparent density aluminum foams varied from 16% to 60% for the continuous specimens and from 2% to 20% for the step-wise specimens. For the 8% density aluminum foams these values were

Table 1
Mechanical properties for continuous and step-wise compression testing of aluminum foam samples

	Cont. test	Std. dev.	Step-wise test	Std. dev.	Percent diff.	*p*-value
4% Al foam samples						
Mass (g)	0.094	0.002	0.092	0.002	1.619	0.776
Apparent density (kg/m^3)	0.125	0.003	0.123	0.003	1.883	0.603
Yield strength (MPa)	0.409	0.090	0.391	0.021	4.330	0.446
Yield strain (%)	1.048	0.584	0.778	0.071	25.829	0.403
Ultimate strength (MPa)	0.475	0.143	0.508	0.014	−6.895	0.882
Ultimate strain (%)	1.927	1.207	2.164	0.444	−12.262	0.643
Ultimate load (N)	22.67	6.73	24.29	0.73	−7.143	0.856
Modulus of elasticity (MPa)	67.3	11.3	68.5	9.4	−1.813	0.905
Stiffness (N/m)	197.0	40.4	207.7	25.5	−5.414	0.968
8% Al foam samples						
Mass (g)	0.164	0.004	0.162	0.004	1.388	0.941
Apparent density (kg/m^3)	0.226	0.008	0.231	0.012	−2.133	0.997
Yield strength (MPa)	1.481	0.102	1.502	0.088	−1.419	0.807
Yield strain (%)	1.776	0.461	1.727	0.615	2.708	0.724
Ultimate strength (MPa)	1.643	0.076	1.636	0.098	0.399	0.549
Ultimate strain (%)	2.710	0.365	2.389	0.425	11.864	0.176
Ultimate load (N)	75.65	5.85	72.97	2.18	3.536	0.518
Modulus of elasticity (MPa)	121.4	17.8	127.6	20.7	−5.094	0.712
Stiffness (N/m)	352.2	44.9	357.6	53.2	−1.534	0.702
12% Al foam samples						
Mass (g)	0.217	0.004	0.217	0.006	0.267	0.864
Apparent density (kg/m^3)	0.298	0.013	0.298	0.019	0.248	0.944
Yield strength (MPa)	2.238	0.318	1.901	0.392	15.036	0.174
Yield strain (%)	1.691	0.243	1.380	0.365	18.412	0.151
Ultimate strength (MPa)	2.449	0.225	2.108	0.379	13.901	0.123
Ultimate strain (%)	2.758	0.369	2.236	0.440	18.921	0.077
Ultimate load (N)	113.2	14.3	98.2	14.6	13.261	0.139
Modulus of elasticity (MPa)	182.9	16.9	185.4	56.5	−1.344	0.928
Stiffness (N/m)	534.0	54.9	563.6	162.7	−5.559	0.709

Table 2
Mechanical properties for continuous and step-wise compression testing of whale bone samples

Whale bone samples	Cont. test	Std. dev.	Step-wise test	Std. dev.	Percent diff.	*t*-test *p*-value
Mass (g)	1.012	0.084	1.005	0.086	0.767	0.862
Apparent density (kg/m^3)	1.292	0.072	1.267	0.074	1.935	0.518
Yield strength (MPa)	14.957	4.084	15.154	4.353	−1.318	0.930
Yield strain (%)	3.010	0.632	3.008	0.553	0.074	0.994
Ultimate strength (MPa)	16.113	3.655	16.185	4.468	−0.447	0.974
Ultimate strain (%)	3.695	0.332	3.434	0.305	7.059	0.122
Ultimate load (N)	781.2	207.9	797.8	255.1	−2.133	0.897
Modulus of elasticity (MPa)	738.8	107.5	693.7	158.6	6.111	0.564
Stiffness (N/m)	2198.5	367.9	2097.7	547.7	4.585	0.708

4–25% for continuous testing, and 5–30% for step-wise testing. CVs for the 12% aluminum foams ranged from 9% to 25% for continuous testing, and from 20% to 30% for step-wise testing.

In Fig. 4, average stress–strain curves for the aluminum and bone cylinders, and the associated standard errors at intervals of 1% strain are presented. Statistical comparisons between the step-wise and continuous tests for the interval strains at 2%, 4%, 8%, 12%, 16%, and 20% showed no significant differences between the curves. Additionally, regression analysis between the two sets of tests yielded a high correlation with r^2 values of 0.98 ($p<0.0001$) for all four sample types. All of the step-wise parameters overlapped with the continuous tests for both the aluminum and bone samples with *p*-values always greater than 0.05.

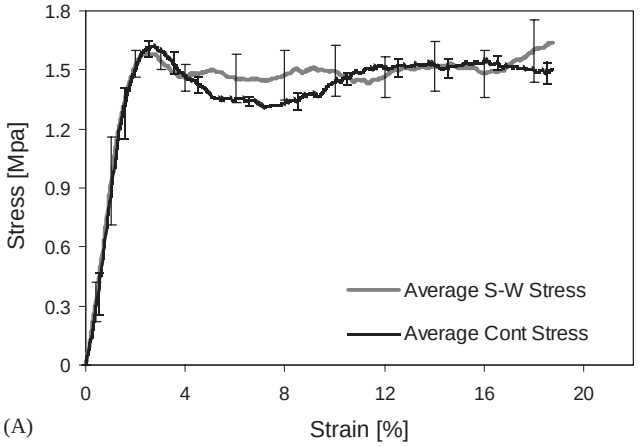

Fig. 4. (A) Average load-strain curve for continuous and step-wise compression of five aluminum specimens. (B) Average load-strain curve for continuous and step-wise compression of five whale bone specimens. Standard deviations were calculated at intervals of 1% strain. The standard error bars are offset by 0.5% for each set of continuous and step-wise curves, in order to prevent overlapping and provide for a clearer visual interpretation.

The "elastic" phases of the continuous and step-wise test curves showed almost identical shape and slope with very similar yield and failure points. There was however a trend towards lower post yield softening stresses in the step-wise test curve. This post-yield softening was more prominent in the "progressive failure" phase of the curve and less prominent at the final "filling" phase. Having performed a strain based step-wise mechanical test, where discrete strain steps were taken and the strains locked on to specimen, stress relaxation is of more importance than creep. As a 20-min waiting period was observed at the end of the application of each strain step, the stress relaxation reached a plateau. This relaxation inherent to the step-wise technique was responsible for the softening stresses in the progressive failure phase of the curve, where trabecular network showed typical "domino effect". Once this phase gives way to the final filling phase, the effects of stress relaxation becomes less prominent. The 20-min waiting period also puts the presumable creep behavior in the secondary "constant" creep rate range. It is worth mentioning that we did not observe any significant changes in the strain and height values observed in a specimen, when the failed specimen was imaged a second time 1 h later.

Figs. 5 and 6 show time-lapsed images obtained from the step-wise micro-compression of a representative aluminum and bone cylinder, respectively. For both types of materials damage was seen to accumulate and propagate in local bands rather than being evenly distributed throughout the structure. In aluminum specimens a general trend of buckling was observed within the structure as a consequence of the imposed strain, where the individual trabeculae throughout the entire specimen tended to bend and buckle. Failure was observed somewhat differently in whale trabecular bone specimens (Fig. 6). Over the imposed strain range of 20%, the top third of the specimen crumbled significantly with the individual trabecular elements experiencing high levels of deformations, whereas the lower part of the specimen remained relatively intact. It can be observed that bone fails in a brittle manner due to the presence of minerals but then shows a very ductile post-failure behavior. It seems that the collagen network within the trabeculae can keep the mineral phase together over a long range of strain. Additionally, in all time-lapsed images failure progression of individual elements could be followed in both the aluminum and bone samples (Fig. 7).

4. Discussion

The use of micro-compression to perform IGFA is a unique technique that allows nondestructive and three-dimensional monitoring of fracture initiation and progression as well as an assessment of local failure mechanisms. Other techniques used to study local failure progression are validated for only small deformations and low nominal strains (around 2%) (Bay, 1995; Kirkpatrick and Brooks, 1998). The overall aim of this project was, first, to develop a micro-mechanical testing system, composed of a MCD and a MTDAQ and, second, to validate and characterize micro-compression together with micro-tomographic imaging so it could be implemented as a standard tool for studying trabecular bone failure well beyond the failure region (up to 20% strain).

With respect to the first aim, a new versatile micro-compression system was designed and successfully implemented. For the validation of the system, aluminum foams, structurally similar to trabecular bone but more predicable in their behavior, as well as whale vertebral bone cores were used. Since mechanical properties will be very sensitive to the experimental

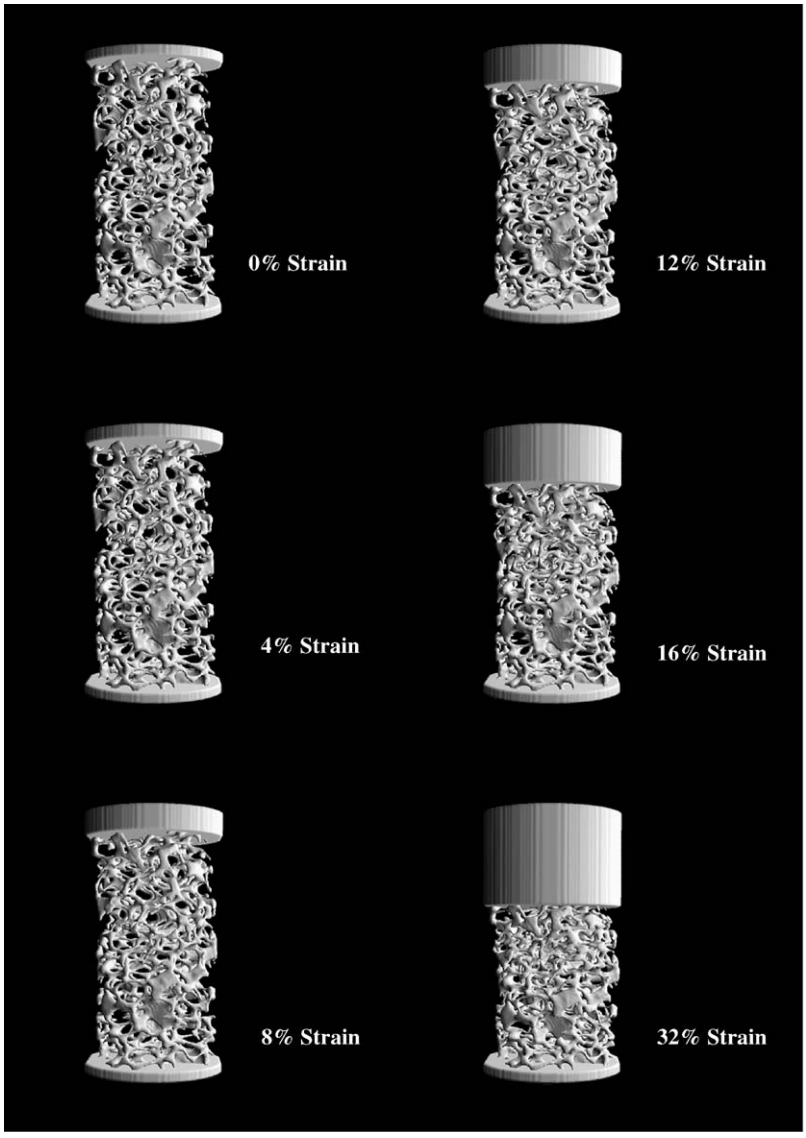

Fig. 5. IGFA of representative 8% aluminum foam. Time-lapsed micro-compression has been performed from 0% to 32%.

setup and the mass, size, and shape of the specimens used, the samples in the aluminum and whale bone test groups were selected to have weights, lengths, and cross-sectional areas that were not statistically significantly different between the two testing protocols. Additionally, the aluminum foam and whale bone specimens were selected to be of uniform mass and density with coefficients of variation of 2% and 8%, respectively. The average divergence of the specimen axis from the predominant direction of the eigenvectors was 4.0° for the whale trabecular bone specimens where plates are predominantly oriented in the vertical direction.

In our study, we found that the general shapes of the stress–strain curves for both continuous and step-wise tests were almost identical for each group. The correlation between continuous and the step-wise testing was very high with 98% of the continuous test behavior, the gold standard, explained by the step-wise compression test. The mechanical properties listed in Tables 1 and 2 were not found to be statistically different for the two test groups ($p > 0.05$). With comparable mechanical properties and a strong correlation between the step-wise and continuous tests, we are confident that step-wise micro-compression is a valid technique to study structural failure mechanisms. Looking at the results from the step-wise compression testing, it is interesting to note that although the standard deviation of mass and density measurements of the tested specimens was only around 2% for aluminum and 8% for bone, the mechanical properties exhibited much higher variations of up to 30% for both aluminum and bone. This indicates that local structural and architectural differences in the samples might have additionally influenced the mechanical behavior of these samples

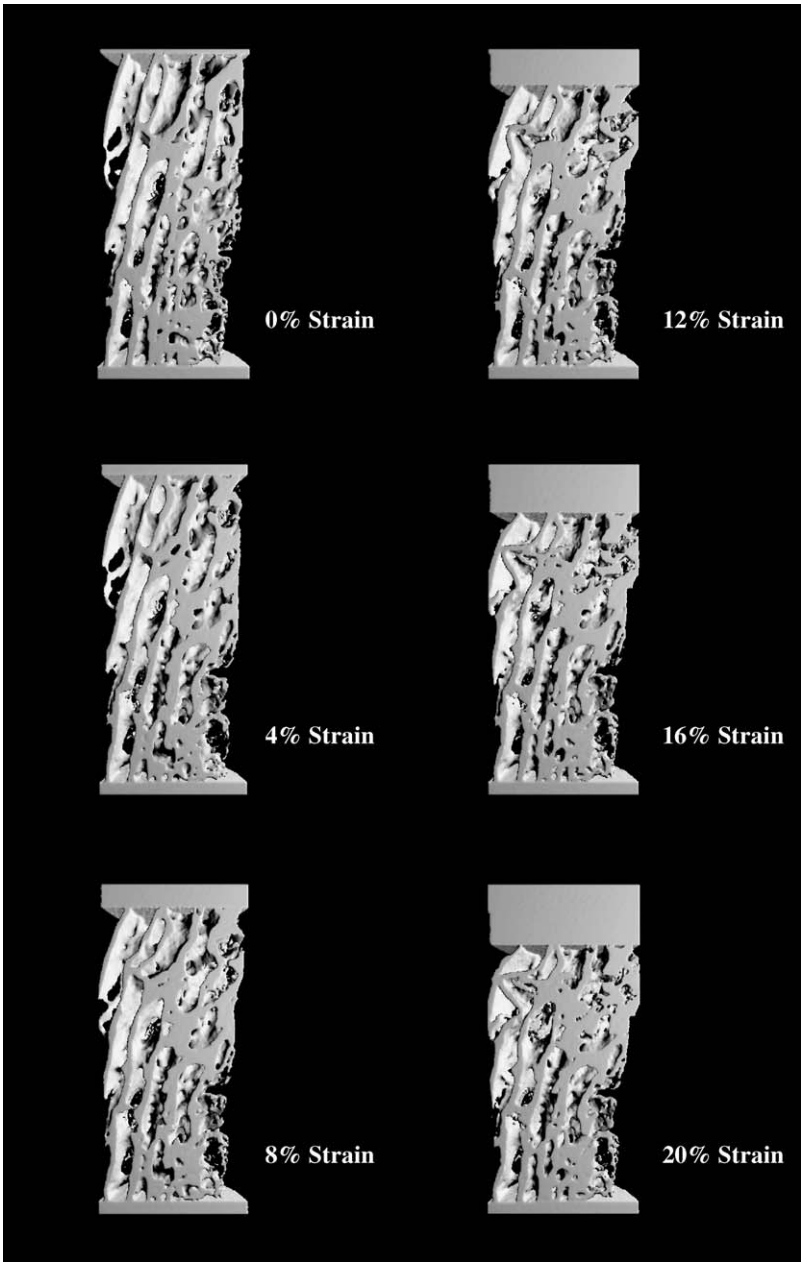

Fig. 6. IGFA of representative whale bone core. Time-lapsed micro-compression has been performed from 0% to 20%.

beyond the simple mass and density relationships. Although established protocols were used in preparation and testing of the specimens in order to minimize artifacts, some of the higher standard deviations observed in mechanical properties could also be attributable to these artifacts. An especially limiting factor of the new system was its displacement measurement system, where the LVDT was attached to the end effector. This in effect measured the total strain, including the specimen strain and the load frame compliance. This was a source of error inherent to the design of our system and was addressed by comparing the nominal strain to the strain measured in the μCT image of the specimen. The average divergence (in parentheses) between the nominal and measured strain steps were as follows: for 2% (0.44%), for 4% (0.67%), for 8% (0.40%) for 12% (0.18%), for 16% (0.21%) and for 20% (0.58%); and the correlation between these two strain measurement was excellent ($r^2 = 1.0$). This limitation could also be a partial reason for the higher than previously reported values for the yield and ultimate strain in this study.

Examining the images in Figs. 5–7 allowed us to monitor failure initiation and progression as well as to detect local structural and architectural differences in the specimens. Nevertheless, the real advantage of

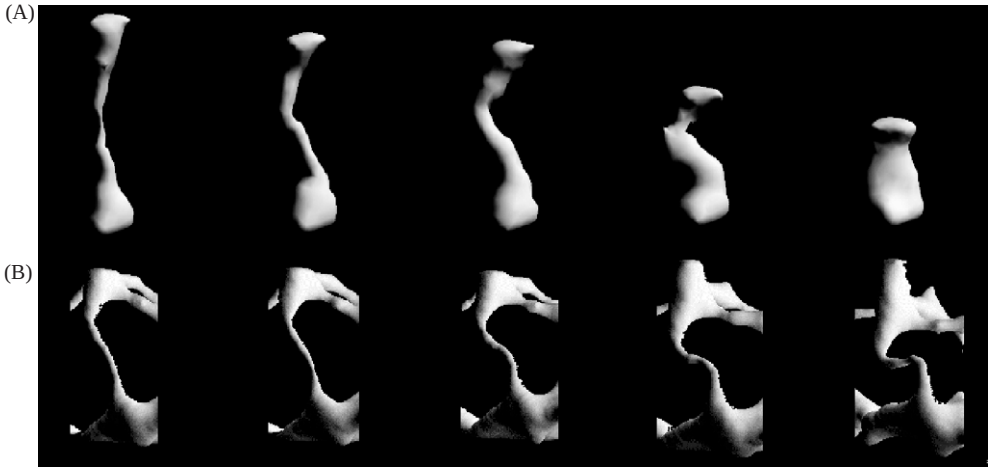

Fig. 7. Image-guided assessment of local failure: (A) rod-like element undergoing large local strain; and (B) although inter-nodal strain can be small, large deformation can occur.

IGFA lays in the possibility to animate fracture initiation and progression to produce movies of structural failure. These animations (see Animations 1–3[1]) revealed that failure occurred in local bands with the remaining regions of the structure largely unaffected. For both the aluminum and whale bone cylinders, buckling failure can be seen in individual elements. Such localized failure of individual elements usually leads to the propagation of structural damage in shear bands. This also implies that local strains may be much larger than the apparent strain exerted on the specimen through the loading mechanism. Once individual elements collapse at one level, the damage propagates to subsequent elements allowing damage to occur throughout the entire structure. In a preliminary study also using whale trabecular bone, similar results were found. Structural failure was described by an initial buckling of the trabeculae followed by a collapse of the overloaded trabeculae (Müller et al., 1998). For the cylinders buckling can also be seen in the overall structure due to the 2:1 ratio between length and diameter (Fig. 5).

In conclusion, micro-compression in combination with three-dimensional μCT allows visualization of failure initiation and propagation in a nondestructive way. In this study, we found step-wise compression to be a valid approach for IGFA with high precision and accuracy as compared to classical continuous testing. However, because the technique was validated using aluminum foams and bone from a single whale vertebra, the reproducibility of the technique for human trabecular bone remains unknown. Also, it is unknown whether the coring technique used to fabricate these cylinders is adequate for obtaining human osteoporotic bone samples. In the future, once these issues are resolved, we hope to address the controversial topic of bone "quality", i.e. whether bone architecture, damage accumulation, and bone mineralization predict structural competence better than bone density alone. The large standard deviations for the mechanical properties of the tested specimens support the notion that density is not the sole factor affecting mechanical properties of bone. We expect these findings to improve our understanding of the relative importance of densitometric, morphological, and loading factors in the etiology of spontaneous fractures of the spine. Eventually, this improved understanding may lead to more successful approaches to the prevention of age-related fractures.

[1] Supplementary data associated with this article can be found at doi:10.1016/S0021-9290(03)00254-9.

Acknowledgements

This study was partly funded by a Biomedical Engineering Research Grant of the Whitaker Foundation and the SNF Professorship in Bioengineering of the Swiss National Science Foundation (FP 620-58097.99). The authors would also like to acknowledge the reviewers for their insightful comments, which could be directly incorporated into this manuscript.

References

Bay, B.K., 1995. Texture correlation: a method for the measurement of detailed strain distributions within trabecular bone. Journal of Orthopaedics Research 13, 258–267.

Choi, K., Goldstein, S.A., 1992. A comparison of the fatigue behavior of human trabecular and cortical bone tissue. Journal of Biomechanics 25, 1371–1381.

Ciarelli, M.J., Goldstein, S.A., Kuhn, J.L., Cody, D.D., Brown, M.B., 1991. Evaluation of orthogonal mechanical properties and density of human trabecular bone from the major metaphyseal regions with materials testing and computed tomography. Journal of Orthopaedic Research 9, 674–682.

Crowell, R.R., Shea, M., Edwards, W.T., Clothiaux, P.L., White, A.A., Hayes, W.C., 1993. Cervical injuries under flexion and compression loading. Journal of Spinal Disorders 6, 175–181.

Goldstein, S.A., 1987. The mechanical properties of trabecular bone: dependence on anatomic location and function. Journal of Biomechanics 20, 1055–1061.

Hildebrand, T., Laib, A., Müller, R., Dequeker, J., Rüegsegger, P., 1999. Direct three-dimensional morphometric analysis of human cancellous bone: microstructural data from spine, femur, iliac crest, and calcaneus. Journal of Bone and Mineral Research 14, 1167–1174.

Kanis, J.A., 1994. Osteoporosis. Blackwell Science Ltd., Oxford, pp. 1–21.

Keaveny, T.M., Borchers, R.E., Gibson, L.J., Hayes, W.C., 1993a. Trabecular bone modulus and strength can depend on specimen geometry. Journal of Biomechanics 26, 991–1000.

Keaveny, T.M., Borchers, R.E., Gibson, L.J., Hayes, W.C., 1993b. Theoretical analysis of the experimental artifact in trabecular bone compressive modulus. Journal of Biomechanics 26, 599–607.

Keaveny, T.M., Guo, X.E., McMahon, T.A., Hayes, W.C., 1994. Trabecular bone exhibits fully linear elastic behavior and yields at low strains. Journal of Biomechanics 9, 1127–1136.

Kleerekoper, M., Villanueva, A.R., Stanciu, J., Rao, D.S., Parfitt, A.M., 1985. The role of three-dimensional trabecular microstructure in the pathogenesis of vertebral compression fractures. Calcified Tissue International 37, 594–597.

Kirkpatrick, S.J., Brooks, B.W., 1998. Micromechanical behavior of cortical bone as inferred from laser speckle data. Journal of Biomedical Materials Research 39, 373–379.

McBroom, R.J., Hayes, W.C., Edwards, W.T., Golddberg, R.P., White, A.A., 1985. Prediction of vertebral body compression fracture using quantitative computed tomography. Journal of Bone and Joint Surgery 67A, 1206.

Michel, M.C., Guo, X.D., Gibson, L.J., McMahon, T.A., Hayes, W.C., 1993. Compressive fatigue behavior of bovine trabecular bone. Journal of Biomechanics 26, 453–463.

Mosekilde, L., 1988. Age-related changes in vertebral trabecular bone architecture—assessed by a new method. Bone 9, 247–250.

Müller, R., Rüegsegger, P., 1997. Micro-tomographic imaging for the nondestructive evaluation of trabecular bone architecture. Studies in Health Technology and Informatics 40, 61–79.

Müller, R., Gerber, S.C., Hayes, W.C., 1998. Micro-compression: a novel technique for the nondestructive assessment of local bone failure. Technology and Health Care 6, 433–444.

Norrdin, R.W., Kawcak, C.E., Capwell, B.A., McIlwraith, C.W., 1998. Subchondral bone failure in an equine model of overload arthrosis. Bone 22, 133–139.

Parfitt, A.M., 1987. Trabecular bone architecture in the pathogenesis and prevention of fracture. American Journal of Medicine 82, 68–72.

Rüegsegger, P., Koller, B., Müller, R., 1996. A microtomographic system for the nondestructive evaluation of bone architecture. Calcified Tissue International 58, 24–29.

Silva, M.J., Keaveny, T.M., Hayes, W.C., 1997. Load sharing between the shell and centrum in the lumbar vertebral body. Spine 22, 140–150.